www.springer.com/41230
https://doi.org/10.1007/s41230-024-4138-y
Research & Development CHINA FOUNDRY
Vol. 22 No. 3 May 2025

Enhanced wear resistance of LDED 316L stainless steel fabricated by in-situ ultrasonic rolling

Yi-gui Su[1], *Guan Liu[1], Xu-yu Pi[1], Dong-xu Wen[2], De-fu Liu[1], and Yong-cheng Lin[1]

1. School of Mechanical and Electrical Engineering, Central South University, Changsha 410083, China

2. State Key Laboratory of Materials Processing and Die & Mould Technology, School of Materials Science and Engineering, Huazhong University of Science and Technology, Wuhan 430074, China

Abstract: Stainless steel parts with complex shape can be fabricated using additive manufacturing, which do not rely on molds and dies. However, coarse dendrites induced by repeated heating of additive manufacturing result in weak properties, which limits its application. In this study, an in-situ ultrasonic rolling (UR) device was developed to assist the laser directed energy deposition (LDED) process. The microstructural characteristics, as well as the microhardness and wear behavior, were studied for the 316L stainless steel manufactured by in-situ ultrasonic rolling assisted LDED. It is found that austenite, ferrite, and small Si oxides are the main constituents of both the LDED and LDED-UR alloy samples. Under the severe plastic deformation of ultrasonic rolling, the long-branched ferrites by LDED are transformed into the rod-like phases by LDED-UR. Meanwhile, the ferrite is more uniformly distributed in the LDED-UR alloy sample compared with that in LDED alloy sample. Columnar grains with the size of 97.85 μm appear in the LDED alloy sample, which is larger than the fully equiaxed grains (22.35 μm) of the LDED-UR alloy. The hardness of the LDED-UR alloy sample is about 266.13±13.62 $HV_{0.2}$, which is larger than that of the LDED alloy sample (212.93±12.85 $HV_{0.2}$). Meanwhile, the wear resistance is also greatly enhanced by applying the assisted in-situ ultrasonic rolling. The achieved high wear resistance can be ascribed to the uniformly distributed hard matter (ferrites) and the impedance of dislocations by high fraction of grain boundaries. Abrasive wear and adhesive wear are identified as the primary wear mechanisms of the studied alloy. Gaining an in-depth understanding of the relationship between wear mechanisms and microstructures offers an effective approach in manufacturing high wear resistant alloys suitable for use in harsh working environments.

Keywords: laser directed energy deposition; ultrasonic rolling; 316L stainless steel; microstructure; wear behavior

CLC numbers: TG142.71 **Document code:** A **Article ID:** 1672-6421(2025)03-301-10

1 Introduction

As a superior engineering material, 316L stainless steel is widely used in aerospace, marine, biomedical and other industries [1-4]. However, 316L stainless steel yields low strength and weak wear resistance under service, which restricts its engineering application [5, 6]. Thus, a high wear resistance of the 316L stainless steel is one of the key evaluation factors in extending its service life under industry applications [7, 8]. Specially, the 316L complicated components with high wear resistance needs innovative manufacturing methods.

***Guan Liu**

Ph. D., Lecturer. His research interests mainly focus on intelligent additive manufacturing.

E-mail: liuguan0811@163.com

Received: 2024-07-03; Revised: 2024-08-06; Accepted: 2024-08-15

Traditionally, the structural components are fabricated via cast, forging, and machining, etc. For the components with complicated shape, the long processing time and multiple processes pose high cost and long time [9-11]. Laser directed energy deposition (LDED) has gained extensive attention as an innovative near-net forming technology in academia and industry, and it is capable for fabricating complex components [12-17].

Many researchers have employed LDED technology to fabricate the 316L stainless steel [18, 19]. Lv et al. [20] studied the relationship between build direction and tensile property of the laser additive manufactured 316L stainless steel, and discovered that a low tensile strength and elongation appeared in normal direction. It can be ascribed to the low density dislocation and small fraction of low angle grain boundaries.

DelRio et al. [21] studied the corrosion behavior of the 316L stainless steel fabricated by laser additive manufacturing, results show that alloys with small porosity and roughness exhibit large breakdown potential. Huang et al. [22] studied the effects of laser power on defects, microstructure, and mechanical properties of the deposited 316L stainless steel, and demonstrated that hot cracks may form at high powers (1,000 W and 2,000 W). Additionally, coarse grains appeared under high laser powers, which resulted in slightly low tensile properties. Laser directed energy deposition technology can be utilized to fabricate 316L stainless steel, however, several challenges such as coarse grains and poor properties, persist in its practical engineering applications.

In order to enhance the properties of 316L stainless steel, two major strategies have been developed. The first is alloy modification. Lee et al. [23] added 1wt.% AlN into 316L steel, and found that the yield strength of the manufactured alloy was increased from 485.4 MPa (without AlN) to 583.2 MPa due to the increased dislocation density. Boron element was employed by Zheng et al. [24] to manufacture 316L/B stainless steel, and the grain size was significantly decreased by increasing the compositional supercooling. Meanwhile, the ultimate tensile strength was enhanced to 1,174 MPa by the refined grains and increased dislocation density. Wang et al. [25] deposited AISI 316L stainless steel by in-situ interstitial N alloying, and discovered that the solidification mode was changed from austenitic-ferritic to fully austenitic. Furthermore, the high strength 316L alloy was fabricated by high density dislocation and interstitial N solid solution. From the above analysis, it is evident that the strength of additive manufactured 316L stainless steel can be enhanced through alloy modification. Nevertheless, the formation of unidentified particles or constituents within the deposited alloys can potentially compromise other properties of the material.

The second is process optimization. Cao et al. [26] studied the effects of scanning speed on fatigue behavior of laser deposited 316L stainless steel, and concluded that the fatigue limit was reduced when the scanning speed exceeded 1,116 $mm \cdot s^{-1}$. Zhang et al. [27] optimized the scan pattern and polar angle during laser additive manufacturing of 316L stainless steel, and highlighted a defect tolerance decided by the morphologies and size of defects. Kim et al. [28] employed the ultrasonic nanocrystalline surface modification (UNSM) to treat the 316L stainless steel manufactured by laser additive manufacturing, and an improved strength and ductility were achieved due to the high dislocation density and grain refinement. Zhang et al. [29] comparatively studied the microstructure characterization before and after hot isostatic pressing processing of the laser additive manufactured 316L stainless steel, results showed that most of the pores were closed, and the cellular structures were eliminated for recrystallization and the growth of grains. Especially, field-assisted [30, 31], heat treatment [32], and other process optimization methods [33, 34] are also employed to enhance the properties of alloys. Among them, plastic deformation assisted method shows positive effects on grains refinement and properties enhancement.

As previously mentioned, a low wear rate is a critical factor for the structural components [35, 36]. Although, the relationship between microstructure and wear behavior has been studied by numerous researchers to uncover the underlying wear mechanisms [37, 38]. Very few studies have been dedicated to elucidate the wear mechanisms of the LDED alloy manufactured by in-situ assisted ultrasonic rolling (UR) technology.

As a novel plastic deformation technology, ultrasonic rolling technology has attracted many attentions [39, 40]. To the best of authors' knowledge, very few publications yield this method to laser directed energy deposition process synchronously. In this work, in-situ ultrasonic rolling assisted LDED (LDED-UR) technology was suggested to enhance the wear resistance of the deposited alloys. The microstructural features and wear resistance were studied for the LDED and LDED-UR alloy samples. An in-depth comprehension of the wear mechanisms addresses a technique guidance for enhancing the wear resistance of the LDED manufactured alloy sample.

2 Experimental procedures

2.1 Powders and substrate

Commercial 316L stainless steel powders (AVIC Maite, China) were employed as feedstock, with an average particle size of approximately 65 μm. Chemical compositions (wt.%) of the investigated 316L alloy are listed in Table 1. The morphology of the 316L stainless steel powders is depicted in Fig. 1(a), and the powder size distribution is illustrated in Fig. 1(b). The powders underwent pre-drying in a desiccator for 12 h at 100 °C. 316L stainless steel plate with a thickness of 16 mm was used as the substrate. Before testing, the oxide film of the plates was polished via #800 to #1500 sandpapers, followed by cleaning with deionized water. To prevent oxidation during processing, 99.99% Ar gas was adopted to protect the melt pool.

2.2 LDED and LDED-UR process

In order to enhance the wear resistance of the deposited alloy, an ultrasonic rolling device was developed to assist the laser directed energy deposition process, as illustrated in Fig. 2. The ultrasonic rolling device was connected to the LDED system via a L-shaped bracket, and then the synchronous manufacturing was realized. Figure 2(b) presents the detailed structure of the developed UR device. It can be seen from Fig. 2(b) that the UR device mainly consists an ultrasonic transducer, an ultrasonic

Table 1: Chemical compositions of the adopted 316L alloy (wt.%)

Elements	Mo	Cr	Mn	Ni	Si	C	Fe
Contents	2.55	17.03	0.45	10.64	0.11	0.024	Bal.

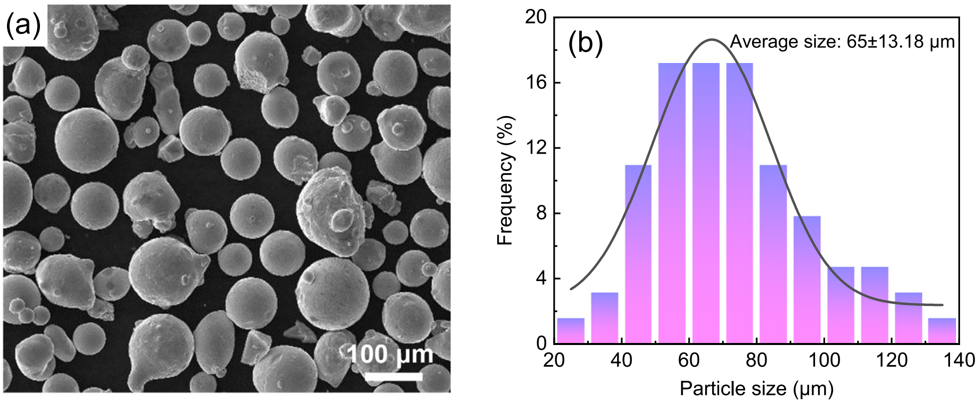

Fig. 1: Powder morphologies (a) and powder size distribution (b)

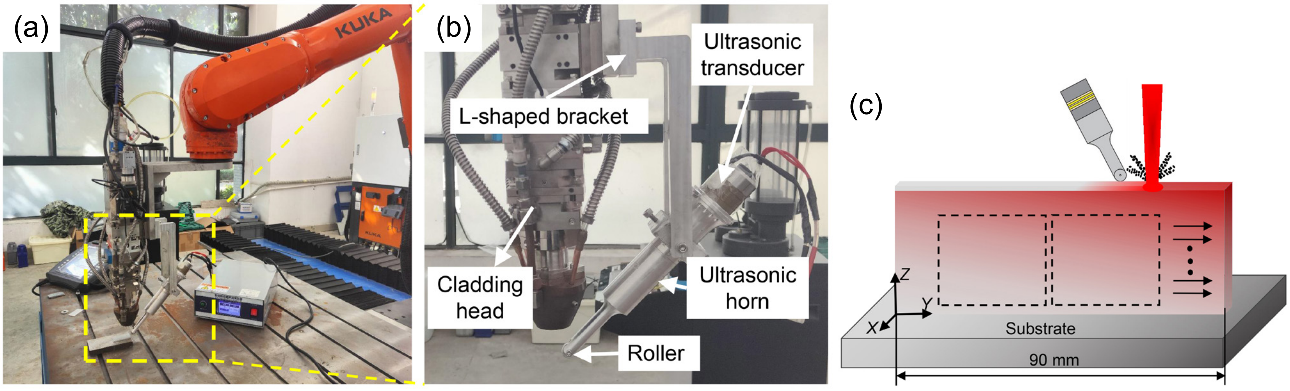

Fig. 2: LDED-UR device (a), detailed structure of ultrasonic rolling set up (b), and schematic of manufacturing process (c)

horn, and a roller. The ultrasonic signal was converted into mechanical vibration by the employed ultrasonic transducer. Then, the ultrasonic horn was designed to amplify and transmit the mechanical vibration to the roller, which was developed to in-situ roll the manufactured alloy samples. Under the LDED and LDED-UR processing, the unidirectional laser scanning strategy was employed, as presented in Fig. 2(c), and a block with the length of 90 mm and height of 60 mm was manufactured.

After a series of optimization experiments, the optimized laser processing parameters were selected and listed in Table 2. For the assisted in-situ UR experiments, the parameters were also optimized, and the results are also shown in Table 2. Note that the optimization experiments was not discussed in this study.

2.3 Microstructure observation

Prior to the microstructural analysis, the samples were ground and polished following the standard protocols. The samples for microstructure observation were cut from the left dotted square of the manufactured alloy, as shown in Fig. 2(c). Microstructural observations were conducted using a Zeiss optical microscope (OM) and a scanning electron microscopy (SEM) system. For OM observation, the samples were chemically etched in a hybrid solution of 30 mL HCl and 10 mL HNO_3 for 20 s. Subsequently, an ultrasonic cleaning device was utilized to clean the etched surfaces to remove the residual corrosion solution.

Table 2: The employed experimental parameters

Parameters	Values
Laser power (W)	1,400
Laser scanning speed ($mm \cdot s^{-1}$)	8
Powder feeding rate ($g \cdot min^{-1}$)	8
Layer thickness (mm)	0.3
Laser spot diameter (mm)	3
Flow rate of the shielding gas ($L \cdot min^{-1}$)	1
Ultrasonic power (W)	600
Ultrasonic frequency (kHz)	20
Distance between laser spot and rolling point (mm)	15

In order to characterize the crystal orientation and texture, the electron backscattered diffraction (EBSD) operation was carried out. The samples for EBSD analysis were previously electrolytically etched in a solution of 10 mL $HClO_4$ and 40 mL C_2H_5OH for 15 s. The Channel 5 software was used to analyze the collected EBSD data. Additionally, the transmission electron microscopy (TEM) operation was employed to further characterize the microstructures, and it was conducted on a TecnaiF30 microscope at 200 kV.

2.4 Properties tests

To determine the hardness of the deposited alloys, Vickers hardness testing (HVS-1000Z, Shanghai, China) was conducted from the bottom to the top of deposited layers with the interval of 1.5 mm (40 points). Meanwhile, these experiments were repeated for three times at a load of 200 g and hold for 10 s.

In order to investigate the wear behavior of the alloys manufactured by LDED and LDED-UR processes, the wear tests were carried out on a ball-on-disk type tribometer (HT-1000, Zhongkekaihua, China) under the ambient temperature of 25 °C and the humidity of 23% (unlubricated dry condition). The samples for wear tests were obtained from the right dotted square of the manufactured sample, as illustrated in Fig. 2(c). Before the dry sliding friction tests, the surfaces of samples were sanded via #800 to #2000 sandpapers, and then polished, ultrasonically cleaned and dried. Due to its superior mechanical properties and thermal stability, Si_3N_4 ceramic balls were selected as the counterpart materials. The experimental parameters according to the ISO 20808: 2016 are listed in Table 3, and three repeated tests were conducted under each case.

The coefficient of friction (CoF) was recorded via the computer system. The three-dimensional wear track surfaces were acquired by the optical profilometer operation (Contour GT-K, Bruker Nano). The wear rate [w, $mm^3 \cdot (N \cdot m)^{-1}$] was calculated by the following expression according to the Archard's law [41]:

$$w = \frac{2 \times 10^{-6} \pi A \cdot r}{F \cdot t \cdot v} \tag{1}$$

where A is the area of the selected section (μm^2), and the other parameters can be found in Table 3.

After conducting the wear tests, SEM images were captured to characterize the worn morphologies, which provide insights into the wear mechanisms.

Table 3: Parameters for wear experimental

Load (F)	Time (t)	Rotation radius (r)	Rotation speed (v)
20 N	30 min	3 mm	94.25 $mm \cdot s^{-1}$

3 Results

3.1 Microstructure

Figure 3 illustrates the SEM micrographs of the LDED and LDED-UR alloy samples. Three different phases, i.e., the matrix phase, the stripe phase, and the spherical phase, can be discovered in Figs. 3(a) and (b). It can be easily seen that the stripe phase in the LDED alloy sample exhibits a long and branched structure, whereas it assumes a rod-like form in the LDED-UR alloy sample. According to the line scanning of the stripe phase, as seen in Fig. 3(c), the enriched elements Cr and Mo appear. Atamert and King [42] proposed that elements Cr and Mo are the stabilizers of the ferrite. Meanwhile, ferrite and austenite are recognized as the principal constituents of the LDED 316L stainless steel [43]. This suggests that the stripe phase is ferrite, and the matrix phase is austenite. It can be seen from Figs. 3(d–f) that the observed spherical phases in both LDED and LDED-UR alloy samples are the Si oxides, which has been detailly analyzed in our earlier study [44], and also aligns with the findings of Wu et al. [45]. By employing the ImageJ software, the average size of Si oxides is measured as 0.29 μm and 0.23 μm for the LDED and LDED-UR alloy samples, respectively, thus the LDED-UR alloy sample exhibits a smaller size of Si oxides.

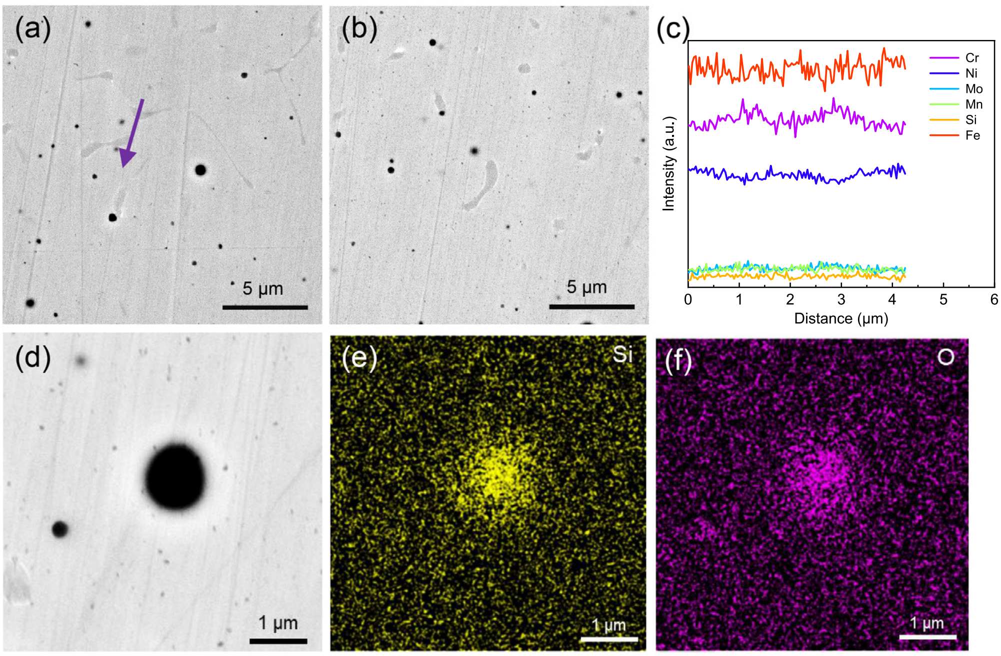

Fig. 3: SEM images of LDED (a) and LDED-UR (b) samples, elemental line scanning of phases in Fig. 3(a) (c) (marked as the arrow), enlarged figure of spherical phase in LDED sample (d), elemental surface scanning of elements Si (e) and O (f)

Figure 4 presents the optical micrographs of the LDED and LDED-UR alloy samples. In Figs. 4(a) and (b), three different regions are obtained along the building direction, and their graphs are illustrated in Figs. 4(a1–a3) and Figs. 4(b1–b3), respectively. From Fig. 4(a), it can be obviously found that columnar grains form in the LDED sample. Meanwhile, slightly difference appears in the enlarged region along the building direction, as presented in Figs. 4(a1–a3). According to Figs. 4(a1–a3), it can also be found that the fraction of dendrites along the building direction is increased, which can be ascribed to the decreased solidification speed. However, for the LDED-UR sample, fully equiaxed grains appear along the building direction, as shown in Fig. 4(b). Meanwhile, the size of equiaxed grains in different zones is similar, which can be obviously detected from Figs. 4(b1–b3).

To further elucidate the grain characteristics of LDED and LDED-UR alloy samples, an EBSD analysis was conducted, and the results are shown in Figs. 5(a) and (b). In the case of the LDED, the columnar grains appear, which is consistent with the findings in Fig. 4(a). Meanwhile, the average grain size of alloy for the LDED is calculated to be 97.85 μm. Under the effects of ultrasonic rolling, the LDED-UR sample exhibits a microstructure with fully equiaxed grains, as depicted in Fig. 5(b). This is also consistent with the optical micrograph results in Fig. 4(b). The average grain size of alloy in the LDED-UR is about 22.35 μm, which is significantly smaller than that of the LDED. Hence, it can be concluded that the grain size can be greatly reduced by the application of ultrasonic rolling, and the fully equiaxed grains are obtained under the in-situ plastic deformation.

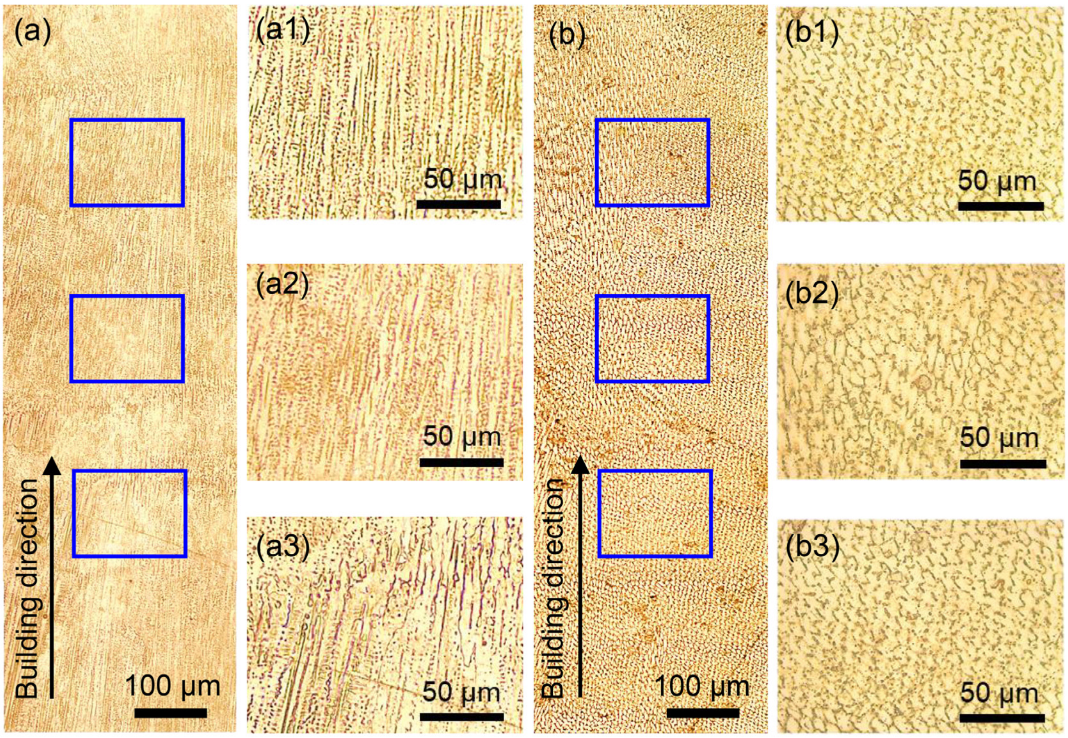

Fig. 4: Optical micrograph of LDED (a) and LDED-UR (b) alloy samples. Note that figures (a1–a3) and (b1–b3) are the local enlarged figures of (a) and (b), respectively

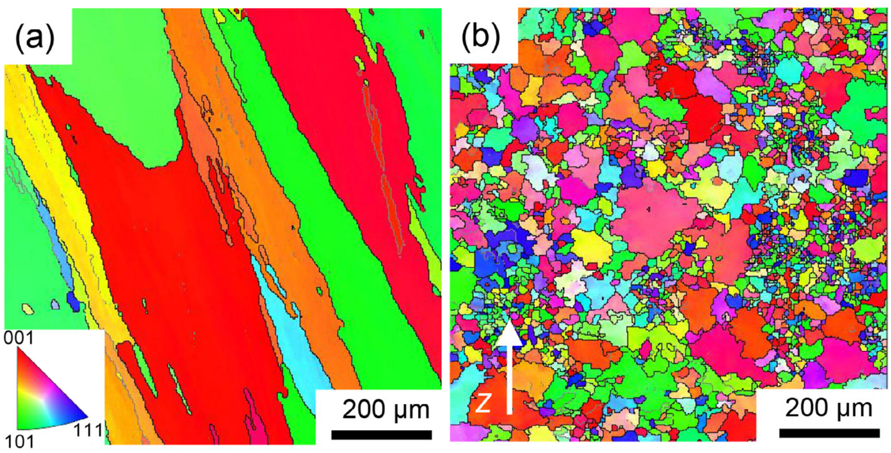

Fig. 5: Grain orientation map of the deposited alloys under LDED (a) and LDED-UR (b) processes

3.2 Microhardness

Microhardness testing was employed to reflect the mechanical properties of the two deposited alloys. Figure 6 illustrates the microhardness values of the LDED and LDED-UR alloy samples, which was measured from the substrate to the top of deposition layers within the *YZ* plane. It can be seen from Fig. 6 that the variation of microhardness does not significantly change along the building direction. The average microhardness for each alloy was calculated. For the LDED alloy sample, the average value is about 212.93±12.85 $HV_{0.2}$, which is smaller than that of the LDED-UR alloy sample (266.13±13.62 $HV_{0.2}$). This discrepancy clearly implies that the microhardness is enhanced by applying in-situ ultrasonic rolling technology. The reason can be ascribed to the refined grains induced by the in-situ ultrasonic rolling approach.

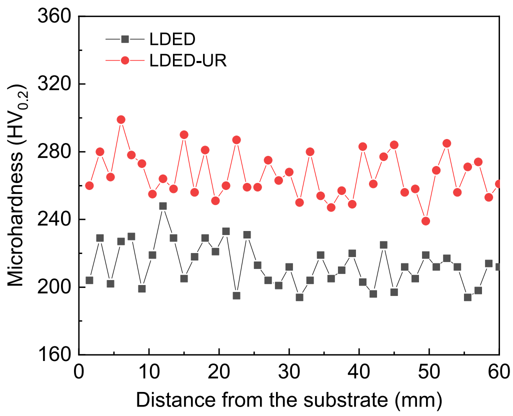

Fig. 6: Microhardness of the alloys under LDED (a) and LDED-UR (b) processes

3.3 Wear resistance

Figure 7 shows the friction coefficient of the LDED and LDED-UR alloy samples. It can be seen from Fig. 7 that the obtained friction coefficient of the LDED alloy sample is about 0.49. When the in-situ ultrasonic rolling is applied on the deposited layers, the friction coefficient is decreased to about 0.4.

In order to characterize the wear behavior of the manufactured alloys, three-dimensional wear tracks were captured by an optical profilometer, as presented in Figs. 8(a–b). Note that the depth profile of the wear tracks can be discerned by the variations in color.

The two-dimensional profiles of the wear tracks are illustrated in Fig. 8(c). It can be obviously seen from Fig. 8(c) that the width and depth of the wear tracks are different for the two samples. The wear track of the LDED-UR alloy sample is notably smaller than that of the LDED alloy sample, suggesting that the sample prepared by LDED-UR possess superior wear resistance than that prepared by LDED possess.

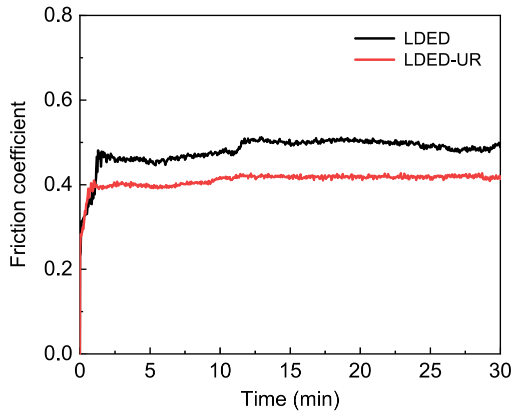

Fig. 7: Friction coefficient of LDED and LDED-UR alloy samples

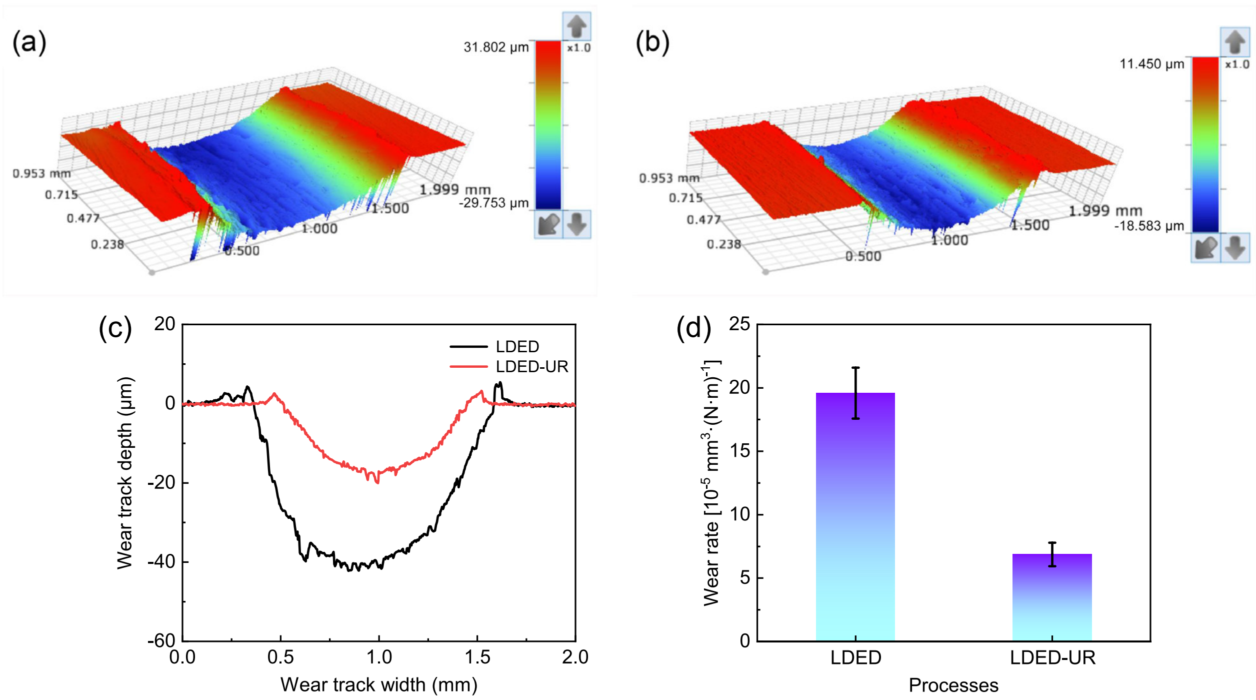

Fig. 8: Three-dimensional profiles of wear track under LDED (a) and LDED-UR (b) processes, two-dimensional profiles of the wear track (c), and the calculated wear rate (d)

In order to quantitatively study the wear behavior of the two samples, the wear rate was calculated according to Eq. (1), and the results of the averaged value of three separate wear tests are illustrated in Fig. 8(d). As presented in Fig. 8(d), the wear rate of the LDED alloy sample is about 19.58×10^{-5} $mm^3\cdot(N\cdot m)^{-1}$, which is significantly higher than that of LDED-UR alloy sample [6.868×10^{-5} $mm^3\cdot(N\cdot m)^{-1}$]. Therefore, it can be conclusively determined that the LDED-UR alloy sample exhibits superior wear resistance.

4 Discussion

4.1 Microstructure analysis

Utilizing in-situ ultrasonic rolling assisted laser directed energy deposition, 316L stainless steel with fully equiaxed grains was successfully manufactured. The microstructural characteristics (including phase attributes and grain size) of the LDED and LDED-UR alloy samples are different, as presented in Figs. 3–5. These differences are indicative of the varying wear resistance between the two alloys. Thus, it is important to carefully address the reason of these microstructural features.

It is recognized that martensitic transformation occurs in 316L stainless steel when subjected to cold deformation [46]. Under the cold deformation, the extent of austenite transforming to martensite depends on the deformation degree (even a relatively low degree, the transformation also occurs). Additionally, the residual austenite will transform to twinning as the strain increases [47]. Based on the SEM images (Fig. 3), EBSD analysis (Fig. 5) and our previous XRD results [48], only ferrite and austenite can be detected in the deposited alloy samples. This implies that the suggested in-situ ultrasonic rolling in this study does not resemble the cold deformation process, such as cold rolling. Prior to the ultrasonic rolling, the insufficient cooling time for the deposited layers will not induce the occurrence of martensitic transformation, which is caused by deformation. It is important to state that undesirable phase transformations in 316L stainless steel are avoided by integrating ultrasonic rolling into the LDED process, which provides a technical strategy for enhancing material properties.

During the LDED-UR process, the plastic deformation caused by ultrasonic rolling occurs at moderately high temperatures. This facilitates the fragmentation of the stripe phases into shorter particles, as illustrated in Fig. 3. Meanwhile, under the intense plastic deformation induced by ultrasonic rolling, the oxides can also be broken down into smaller ones. Except the decreased size of phases, the average grain size of LDED-UR alloy sample is also deceased. That is the reason why the structures of samples in the LDED-UR process are smaller than those in the LDED process.

In the LDED process, rapid melting and solidification occur, and the dendrites preferentially grow in the orientation <001>, which has been detailly discussed by numerous researchers [49]. In the LDED-UR process, ultrasonic vibration and plastic deformation induced by roller are the two major contributors to the reduction of grain size. Prior to the action of roller, the fluidity of the melt pool and mushy zone can be enhanced by the synergistic effect of cavitation and acoustic streaming, which is induced by ultrasonic vibration. Simultaneously, numerous microscopic bubbles (it can be indicated by pores in Fig. 9) are generated. When a critical level of the sound pressure is reached, these tiny bubbles expand rapidly, and then collapse abruptly, generating substantial shockwave energy within the melt pool and mushy zone. This energy results in the fragmentation and detachment of columnar grains, which provide nucleation sites for the formation of equiaxed grains.

The huge rolling pressure exerted by the roller induces severe plastic deformation, which leads to the generation of dislocations. Meanwhile, a high density of dislocation emerges under the combined influence of the ultrasonic energy field, cyclic thermal field, and plastic deformation. Then, the generated dislocations rapidly glide and coalesce within a short time. This merging of dislocations results in the formation of small angle grain boundaries that eventually transform into new grain boundaries [50, 51]. This dynamic recrystallization process further refines the equiaxed grains, contributing to a more refined microstructure.

4.2 Wear mechanisms

For an in-depth study on the wear mechanisms of these alloys, the worn surface morphology after wear tests were observed, as illustrated in Fig. 10. Comparing Figs. 10(a) and (c), it can be easily seen that the wear track of the LDED alloy is broader than that of the LDED-UR alloy. The magnified views in Figs. 10(b) and (d) reveal plowing grooves and fragments on the worn surfaces, suggesting a predominant wear mechanism of abrasive wear. Notably, the amounts of fragments on the worn surfaces are different for the two samples. High fraction

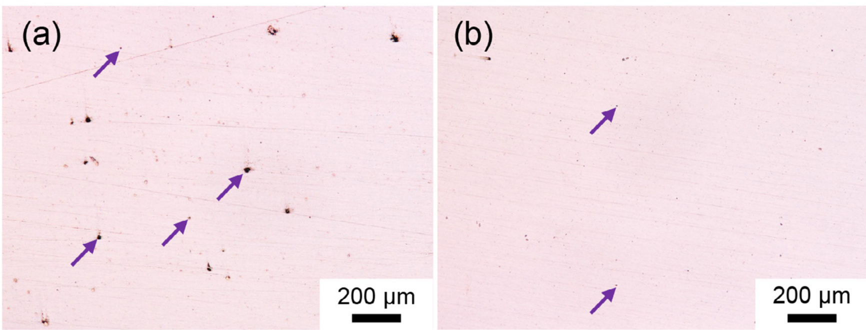

Fig. 9: Optical micrograph of LDED (a) and LDED-UR (b) alloy samples. Note that the arrows refer to the pores

of fragments can be observed on the worn surface of the LDED alloy sample, as seen in Fig. 10(a). This implies a high wear rate and a bad wear resistance of the LDED alloy sample, as shown in Fig. 8(d). For the LDED-UR alloy sample, the worn surfaces exhibit only few fragments, as presented in Fig. 10(c). It can be inferred that the in-situ ultrasonic rolling-assisted LDED alloy sample possesses superior wear resistance. Additionally, a few adhesions can also be detected, implying the existence of adhesive wear.

It is widely acknowledged that the wear resistance of alloys is closely related to their hardness, i.e., high hardness generally correlates with the improved wear resistance [46]. In this study, this relationship has also been proved. As illustrated in Fig. 3, the ferrite phase exhibits varying sizes. Under the plastic deformation of ultrasonic rolling, ferrite is relatively uniformly distributed within the austenite matrix. Given its superior wear resistance, ferrite plays a significant role during the wear process. Meanwhile, the softer austenite matrix is susceptible to wear, leading to the formation of debris on the worn surfaces. During the wear process, the hard matter (the ferrite) acts as a hard-skeleton support, which facilitates the load transfer from the soft matrix to the hard ferrite. In the LDED-UR alloy sample, the ferrite is relatively uniformly distributed in the matrix, which can effectively protect the matrix from ploughing. Thus, the LDED-UR alloy sample with uniformly distributed ferrite demonstrates superior wear resistance. Additionally, the presence of fine equiaxed grains also contributes to enhancing the wear resistance of the LDED-UR alloy sample. In the LDED-UR alloy sample, fine equiaxed grains indicate the high fraction of grain boundaries, which impede the movement of dislocations and plastic deformation. The impedance of dislocations by grain boundaries can be found in Fig. 11. This leads to that the strain-hardened tribolayer forms on the worn surface, and then the contact between friction pairs is reduced. Finally, the wear of the surfaces is greatly reduced, i.e., the enhanced wear resistance.

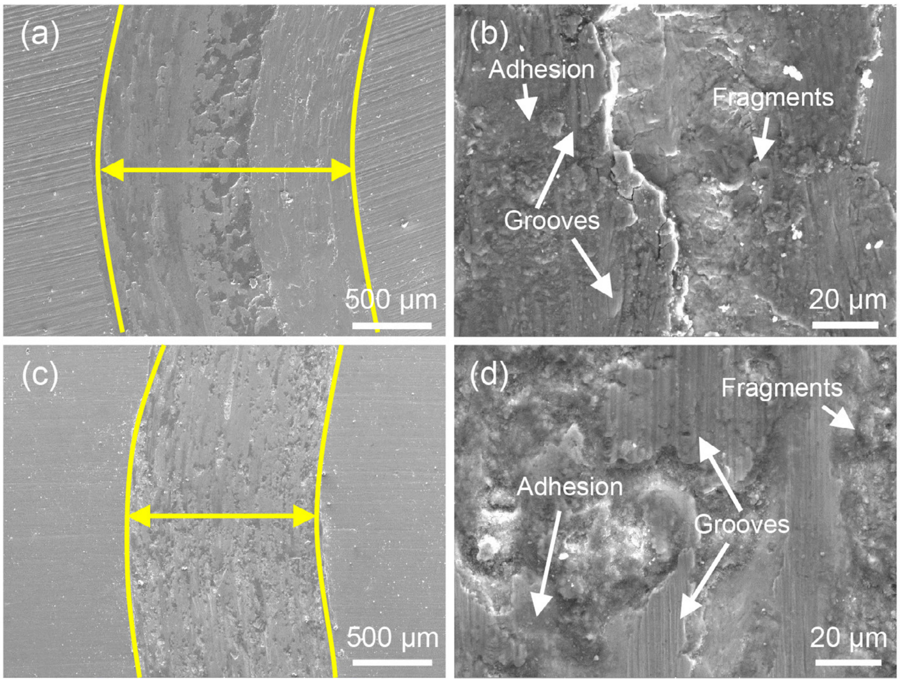

Fig. 10: Morphology of the worn surface under LDED (a, b) and LDED-UR (c, d) processes

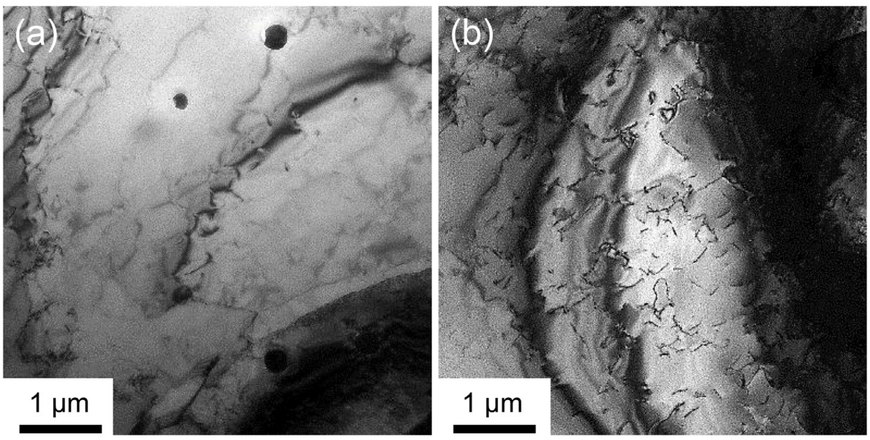

Fig. 11: TEM micrographs of LDED (a) and LDED-UR (b) alloy samples

5 Conclusions

An innovative in-situ ultrasonic rolling apparatus was developed and installed in a LDED operation, which allows each deposited layers deformed synchronously. The microstructural characterization and wear behavior of the 316L stainless steel prepared by LDED and LDED-UR processes were investigated in this study. The findings are concluded as follows:

(1) Austenite, ferrite, and Si oxides are the major structures of the deposited alloys. The ferrite in LDED-UR alloy sample is rolled, resulting in its small size and relatively uniform distribution. Columnar grains with the size of 97.85 μm appear in the LDED alloy sample. Fully equiaxed grains are obtained in LDED-UR alloy sample, and their size (22.35 μm) is far smaller than that of the LDED alloy sample.

(2) The microhardness of the LDED-UR alloy sample is 266.13±13.62 $HV_{0.2}$, which is far larger than that of the LDED alloy sample (212.93±12.85 $HV_{0.2}$). The wear rate of the LDED alloy sample is about 19.58×10^{-5} $mm^3\cdot(N\cdot m)^{-1}$, which is far greater than that of LDED-UR alloy sample [6.868×10^{-5} $mm^3\cdot(N\cdot m)^{-1}$]. The LDED-UR alloy sample presents superior wear resistance.

(3) The abrasive wear and the adhesive wear are the main wear mechanisms for the LDED and LDED-UR alloy samples. The superior wear resistance of the LDED-UR alloy sample is related to the uniformly distributed hard matter with small sizes and the fine equiaxed grains.

Acknowledgments

Financial supports from the National Natural Science Foundation of China (No. 52305440), the Natural Science Foundation of Changsha City (Nos. kq2208272, kq2208274), the Tribology Science Fund of the State Key Laboratory of Tribology in Advanced Equipment (No. SKLTKF22B09), and the National Key Research and Development Program of China (No. 2022YFB3706902) were acknowledged.

Conflict of interest

The authors declare that they have no known competing financial interests or personal relationships that could have appeared to influence the work reported in this paper.

References

[1] Ma M M, Wang Z M, Zeng X Y. A comparison on metallurgical behaviors of 316L stainless steel by selective laser melting and laser cladding deposition. Materials Science & Engineering: A, 2017, 685: 265–273.

[2] Cai Y, Lu T, Ma G D, et al. Effects of geometrical characteristics on defect distributions in alloy components produced by selective laser melting. China Foundry, 2021, 18(4): 369–378.

[3] Yildiz R A, Popa A A, Malekan M. On the effect of small laser spot size on the mechanical behaviour of 316L stainless steel fabricated by L-PBF additive manufacturing. Materials Today Communications, 2024, 38: 108168.

[4] Liu G, Su Y G, Pi X Y, et al. Fatigue strength improvement of laser-directed energy deposition 316L stainless steel with in situ ultrasonic rolling by preliminary investigation. Materials, 2024, 17(15): 3693.

[5] Luo K Y, Xu S K, Xu L J, et al. Wear behaviors of AISI 316L stainless steel with a gradient structured surface layer induced by laser shock peening. Surface & Coatings Technology, 2024, 481: 130608.

[6] Wei Y P, Yang H, Cheng J C, et al. Compression behavior of 316L lattice structures produced by indirect additive manufacturing. China Foundry, 2023, 20(2): 83–88.

[7] Mandal A, Tiwari J K, Almangour B, et al. Tribological behavior of graphene-reinforced 316L stainless-steel composite prepared via selective laser melting. Tribology International, 2020, 151: 106525.

[8] Yue X, Hu S, Yin F, et al. Understanding the wear behavior and mechanism of gradient nanostructured M50 bearing steel through nanoscratching tests. Materials Today Communications, 2024, 39: 109235.

[9] Zhang S, Lin Y C, Jiang Y Q, et al. Accurate simulation of texture evolution and mechanical response of cubic and hexagonal structural alloys using self-consistent polycrystal plastic method. Journal of Alloys and Compounds, 2024, 987: 174191.

[10] Chen X M, Ning M T, Hu H W, et al. Investigation on microstructural and microhardness evolution of GH4698 superalloy under transiently varying strain rates. Materials Science & Engineering: A, 2024, 892: 146014.

[11] Yang Q M, Lin Y C, Zhao W W, et al. Formation and elimination mechanisms of prior particle boundaries in a new powder metallurgy superalloy. Journal of Materials Research and Technology, 2023, 27: 8037–8049.

[12 Liu G, Du D, Wang K M, et al. High-temperature oxidation behavior of a directionally solidified superalloy repaired by directed energy deposition. Corrosion Science, 2021, 193: 109918.

[13] Liu G, Du D, Wang K M, et al. Microstructure and nanoindentation creep behavior of IC10 directionally solidified superalloy repaired by laser metal deposition. Materials Science & Engineering: A, 2021, 808: 140911.

[14] Zhu M L, Jin L, Xuan F Z. Fatigue life and mechanistic modeling of interior micro-defect induced cracking in high cycle and very high cycle regimes. Acta Materialia, 2018, 157: 259–275.

[15] Zhang H M, Wu Y J, Wang Y, et al. In-situ nanoscale precipitation behavior and strengthening mechanism of WC/IN718 composites manufactured by laser powder bed fusion. Composites, Part B: Engineering, 2024, 284: 111727.

[16] Chen M R, Luo S C, Chen X M, et al. Effect of deposition parameters and deposition height on the microstructure and properties of laser-cold metal transfer composite additively manufactured 2319 aluminum alloy. Materials, 2024, 17(12): 2914.

[17] Luo M J, Li R D, Zheng D, et al. Formation mechanism of inherent spatial heterogeneity of microstructure and mechanical properties of NiTi SMA prepared by laser directed energy deposition. International Journal of Extreme Manufacturing, 2023, 5(3): 35005.

[18] Zhang L, Zhai W G, Zhao K, et al. Enhanced quasi-static and dynamic tensile properties of stainless steel 316L produced by laser aided additive manufacturing in controlled argon environment. Materials Science & Engineering: A, 2024, 895: 146255.

[19] Dong S Y, Zhao X, Yan S X, et al. Tailoring microstructure evolution and mechanical properties of a high-performance alloy steel through controlled thermal cycles of a direct laser depositing process. China Foundry, 2021, 18(5): 463–473.

[20] Lv J L, Zhou Z P, Wang Z Q, et al. The effect of build orientation on tensile properties and corrosion resistance of 316L stainless steel fabricated by laser powder bed fusion. Journal of Manufacturing Processes, 2023, 106: 363–369.
[21] DelRio F W, Khan R M, Heiden M J, et al. Porosity, roughness, and passive film morphology influence the corrosion behavior of 316L stainless steel manufactured by laser powder bed fusion. Journal of Manufacturing Processes, 2023, 102: 654–662.
[22] Huang G, Wei K W, Deng J F, et al. High-power laser powder bed fusion of 316L stainless steel: Defects, microstructure, and mechanical properties. Journal of Manufacturing Processes, 2022, 83: 235–245.
[23] Lee S H, Chung S G, Kim H S, et al. Effects of AlN addition into AISI 316L on melt pool stability and microstructural evolution during laser powder bed fusion. Materials Science & Engineering: A, 2023, 881: 145311.
[24] Zheng Q, Chen H S, Zhou J, et al. Effect of boron element on microstructure and mechanical properties of 316L stainless steel manufactured by selective laser melting. Journal of Materials Research and Technology, 2023, 26: 3744–3755.
[25] Wang Z D, Li R, Chen M Z, et al. Enhanced wear and corrosion resistance of the laser direct metal deposited AISI 316L stainless steel by in-situ interstitial N alloying. Optics and Laser Technology, 2024, 171: 110381.
[26] Cao Y F, Moumni Z, Zhu J H, et al. Effect of scanning speed on fatigue behavior of 316L stainless steel fabricated by laser powder bed fusion. Journal of Materials Processing Technology, 2023, 319: 118043.
[27] Zhang J, Zeißig M, Dörfert R, et al. Influence of laser beam scanning pattern and polar angle on the fatigue behavior of additively manufactured specimens made of steel 316L. Materials Science & Engineering: A, 2023, 886: 145651.
[28] Kim R E, Jeong S G, Ha H, et al. Controlling defects of laser-powder bed fusion processed 316L stainless steel via ultrasonic nanocrystalline surface modification. Materials Science & Engineering: A, 2023, 887: 145726.
[29] Zhang S T, Bi F Q, Wu T, et al. Microstructural investigation of the effect of hot-isostatic-pressing treatment on a laser powder bed fused type 316L stainless steel. Materials Characterization, 2023, 197: 112716.
[30] Ouyang W T, Xu Z F, Chao Y, et al. Effect of electrostatic field on microstructure and mechanical properties of the 316L stainless steel modified layer fabricated by laser cladding. Materials Characterization, 2022, 191: 112123.
[31] Wu P F, Hirtler M, Bambach M, et al. Effects of build- and scan-directions on magnetic field-assisted finishing of 316L stainless steel disks produced with selective laser melting. Cirp Journal of Manufacturing Science and Technology, 2020, 31: 583–594.
[32] Zhang Z, Zhao Z Y, Li X F, et al. Effect of heat treatments on metastable pitting of 316L stainless steel fabricated by selective laser melting. Journal of Materials Research and Technology, 2022, 21: 1903–1914.
[33] Zhang Z L, Zhi G, Liu Y, et al. Microstructure and properties nonuniformity of Ti6Al4V component fabricated by high-power laser melting deposition. Materials Science & Engineering: A, 2024, 902: 146604.
[34] Niu P D, Li R D, Gan K F, et al. Manipulating stacking fault energy to achieve crack inhibition and superior strength-ductility synergy in an additively manufactured high-entropy alloy. Advanced Materials (Weinheim), 2024: e2310160.
[35] Liu G, Su Y G, Xin S W, et al. Enhanced wear resistance of Ti reinforced Inconel 718 superalloy manufactured by laser directed energy deposition. Materials Characterization, 2024, 209: 113736.
[36] Liu G, Du D, Wang K M, et al. Microstructure and wear behavior of IC10 directionally solidified superalloy repaired by directed energy deposition. Journal of Materials Science & Technology, 2021, 93: 71–78.
[37] Chen G D, Liu X B, Zhang F Z, et al. Refractory ceramic WC reinforced Co matrix composite coatings on IN718 superalloy: Microstructure, wear mechanisms and surface energy. Tribology International, 2024, 194: 109516.
[38] Chen G D, Liu X B, Zhang F Z, et al. Fabrication and tribological properties of laser cladding WC-Cu/Co-based composite coatings. Surface & Coatings Technology, 2023, 472: 129930.
[39] Wu D B, Zheng Y, Wang H, et al. Formation mechanism of nano-crystal on the blade surface produced by low-plasticity ultrasonic rolling strengthening process. Journal of Manufacturing Processes, 2023, 90: 357–366.
[40] Yang J, Liu D X, Li M Y, et al. Evolution mechanism for a surface gradient nanostructure in GH4169 superalloy induced by an ultrasonic surface rolling process. Materials Science & Engineering: A, 2023, 879: 145271.
[41] Liu J, Liu D F, Li S C, et al. The effects of graphene oxide doping on the friction and wear properties of TiN bioinert ceramic coatings prepared using wide-band laser cladding. Surface & Coatings Technology, 2023, 458: 129354.
[42] Atamert S, King J E. Elemental partitioning and microstructural development in duplex stainless steel weld metal. Acta Metallurgica et Materialia, 1991, 3(39): 273–285.
[43] Zhong Y, Zheng Z Z, Li J J, et al. Effect of in-situ transverse magnetic field on microstructure, mechanical properties and corrosion resistance of the directed energy deposited 316L stainless steel. Additive Manufacturing, 2023, 68: 103508.
[44] Liu G, Su Y G, Pi X Y, et al. Enhanced electrochemical corrosion resistance of 316L stainless steel manufactured by ultrasonic rolling assisted laser directed energy deposition. China Foundry, 2024. https://doi.org/10.1007/s41230-024-4090-x
[45] Wu D J, Yu C S, Wang Q Y, et al. Synchronous-hammer-forging-assisted laser directed energy deposition additive manufacturing of high-performance 316L samples. Journal of Materials Processing Technology, 2022, 307: 117695.
[46] Kan W H, Jiang D R, Humbert M, et al. Effect of in-situ layer-by-layer rolling on the microstructure, mechanical properties, and corrosion resistance of a directed energy deposited 316L stainless steel. Additive Manufacturing, 2022, 55: 102863.
[47] Nezakat M, Akhiani H, Hoseini M, et al. Effect of thermo-mechanical processing on texture evolution in austenitic stainless steel 316L. Materials Characterization, 2014, 98: 10–17.
[48] Liu G, Su Y G, Pi X Y, et al. Achieving high strength 316L stainless steel by laser directed energy deposition-ultrasonic rolling hybrid process. Materials Science & Engineering: A, 2024, 903: 146665.
[49] Liu G, Du D, Wang K M, et al. Epitaxial growth behavior and stray grains formation mechanism during laser surface re-melting of directionally solidified nickel-based superalloys. Journal of Alloys and Compounds, 2021, 853: 157325.
[50] He D G, Xie H, Lin Y C, et al. High-temperature compression behaviors and constitutive models of a 7046-aluminum alloy. Materials (Basel), 2023, 16(19): 6412.
[51] Wen D X, Lin Y C, Li X H, et al. Hot deformation characteristics and dislocation substructure evolution of a nickel-base alloy considering effects of δ phase. Journal of Alloys and Compounds, 2018, 764: 1008–1020.